KSME

Springer

Journal of Mechanical Science and Technology 35 (11) 2021

Original Article
DOI 10.1007/s12206-021-1025-y

Keywords:
· Polymer
· Enzyme-triggered decrystallization
· Chemomechanical model

Correspondence to:
Yiqi Mao
maoyiqi1984@163.com

Citation:
Yang, X., Yang, C., Hou, S., Mao, Y. (2021). Micromechanical modeling for viscoplastic properties of enzyme degradable semi-crystalline poly(ε-caprolactone). Journal of Mechanical Science and Technology 35 (11) (2021) 5081~5097. http://doi.org/10.1007/s12206-021-1025-y

Received December 24th, 2020
Revised February 15th, 2021
Accepted April 26th, 2021

† Recommended by Editor Hyun-Gyu Kim

Micromechanical modeling for viscoplastic properties of enzyme degradable semi-crystalline poly (ε-caprolactone)

Xinwei Yang, Cheng Yang, Shujuan Hou and Yiqi Mao

Department of Engineering Mechanics, College of Mechanical and Vehicle Engineering, Hunan University, Changsha, Hunan, China

Abstract This work provide theoretical understandings for the enzyme-degradable PCL, and assist its structural designs and engineering applications. An energy-dependent evolution model is developed to reflect the enzyme-triggered decrystallization of crystals and the further dissolution by applying a chain-broken chemical reaction. Then, the mechanical properties of the enzyme-degradable semicrystalline PCL is modelled through the homogenization-based procedure by the volume-average of a collection of laminated inclusions with crystals and amorphous phase. A dual-phase-lag diffusion model is advanced to solve the enzyme concentrations in the PCL. The model is calibrated by the experiments and then applied for the chemomechanical properties of the PCL when under enzyme conditions. Some numerical examples are conducted to discuss effects of the enzyme concentration and the crystallinity on the crystallographic axe evolution as well as the overall chemomechanical properties of the semicrystalline PCL.

1. Introduction

Characterized with merits of high biocompatibility, enzyme-degradationability and non-toxicity, the poly(ε-caprolactone) (PCL) and the PCL-constituent composite find a wide potential applications in biomedical and pharmaceutical industries, such as biological scaffold [1], bone regeneration [2], drug delivery application [3], regeneration of healing tissues [4] and etc. Among these bio-applications, the structural integrities and the mechanical strengths of the PCL-constituent composites and structures are thus very important for the stable and regular engineering performances. The poly(ε-caprolactone) (PCL), a typical semi-crystalline material, consists of two phases, i.e., crystalline phase and amorphous phase, where the crystal phase ensures the sufficient mechanical strength, while the amorphous phase provides the material ductility. In addition, the crystals undergo melt-crystallization transitions when under temperature variation and enzyme-activated degradation, where dramatic modulus contrast of the crystalline phase and amorphous phase provides a wide design space of the PCL-constituent composites/structures. For example, Buffington et al. [5] recently developed an enzyme degradable shape memory polymer (EDSMP) by utilizing the heat-enzyme activated crystal-melt transition of the PCL. This new design develops a new trigger for shape memory (SM) effect of polymers, and finds a wide biological and medical applications by introducing the SM capacities to enzyme-activated materials, such as tissue regeneration, drug delivery, wound healing, etc. What is more, the chemo-triggered melt-crystal transition of the PCL provides a feasible approach for designing a wide series of intelligent polymer composites having different chemistries to achieve applications in bioengineering. More engineering applications by applying the dissolution of semicrystalline polymers can be found on membrane science [6], recycling of polymers [7], controlled drug delivery [8], and etc. Therefore, it is of great importance to get a deep understanding on the enzyme-triggered decrystallization of the PCL, as well as the overall

chemomechanical behaviors of the PCL and PCL-constituent composites and structures.

Lots of experimental works can be found on the analysis of dissolution of polymers [9]. In contrast, only few theoretical works can be found on the dissolution properties and coupled chemo-mechanical behaviors of polymer. Herman and Edwards [10] developed a linear dissolution model for amorphous polymer, in which the swelling properties of the material under immersion were included. Later, Kaunisto et al. [11] proposed a more efficient mathematical model for the dissolution of a polyethylene oxide tablet. These models are applicable for analysis of 1D diffusion and dissolution of polymer, and more 1D models can be referred to Refs. [6, 12, 13]. Different from the dissolution mechanisms of amorphous polymer, it was believed there are three molecular mechanism steps in dissolution of semicrystalline polymer, i.e., decrystallization, cleavage of chain networks and the further chain diffusion [14]. For example, Hassan et al. [15] analyzed the dissolution properties of crystals based on a three-step dissolution kinematics for the semicrystalline PVA gels. Recently, a 3D dissolution has been developed by Yu et al. [16], where the dissolution model was developed for polymer based on bond exchange reaction (BER), and micromechanism of polymer chains were considered in dissolution process. For the coupled chemo-thermomechanical analysis of the PCL-constituent composites, a more elaborated 3D theoretical model is needed for semicrystalline PCL to get a deep understanding of the enzyme/thermal triggered dissolution kinematics.

When cooled from the melt, semicrystalline polymers regularly exhibit spherulitic morphologies comprising radial arrangements of broad thin crystalline lamellae infilled with amorphous layers, and the overall chemo-thermomechanical properties depend on the local properties of the constituents and crystallographic evolutions [17-21]. The homogenization-based method was demonstrated effective on well predicting overall properties of semicrystalline polymers with detailed description of micro-features, as done in the works [18, 20, 22-27]. In these homogenization-based procedures, the overall properties of each representative volume element (RVE) were solved by volume-averaged results over an assemble of two-layer laminated composite inclusions with randomly distributed interface normal directions. Based on the homogenization-based approaches [7, 20], we develop a viscoplastic model for the PCL when under enzyme-activated decrystallization and dissolution. The kinematic models are developed for the enzyme-activated decrystallization of crystals, as well as the further dissolution process of the amorphous chains. Then, a homogenization-based model is proposed for the overall chemomechanical properties of the PCL. Following the procedures in the works [7, 20], the macro-material properties of the semicrystalline PCL are solved from the nested representative volume element (RVE) containing multi-inclusions, with each inclusion a laminated composite of amorphous layer and crystalline layer. In the remainder of this work, the Sec. 2 describes the material and experimental methods for characterizing enzyme diffusion and the mechanical properties of the enzyme-degraded PCL. Sec. 3 presents the developed homogenization-based viscoplastic model for the PCL under enzyme degradation. In Sec. 4. the model is calibrated by experiments; some numerical examples and discussions are presented.

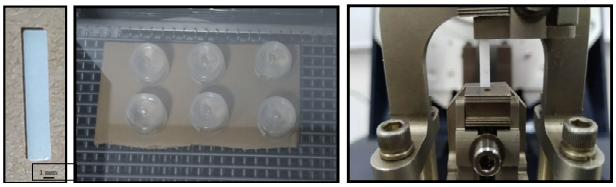

(a) (b) (c)

Fig. 1. (a) The tested PCL strip; (b) the PCL strips are immersed in enzyme solutions and the containers are put in the sterile oven; (c) the mechanical properties of the PCL strips are tested by DMA.

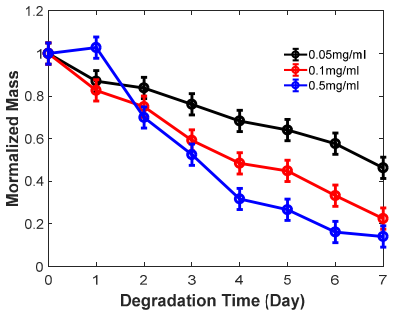

Fig. 2. Normalized mass variations of the PCL strips along with immersion time when under enzyme degradation.

2. Materials and experiments

2.1 Materials and experimental setups

The poly(ε-caprolactone) (PCL) slices were printed by a 3D printer, and then cut into strips of 12 mm(L)×2 mm(W)×0.47 mm(H), as presented in Fig. 1(a). The enzyme solutions were synthesized by dissolving enzyme powders into pure water. Three concentrations of 0.05 mg/ml, 0.1 mg/ml and 0.5 mg/ml were prepared. The PCL strips were immersed in the enzyme solutions, and the enzyme solution containers were put in the sterile oven at room temperature to ensure the enzyme activities, as presented in the Fig. 1(b). Then, the immersed samples were taken out to test the weights using the electronic microbalance after wiping excess enzyme solution from the surface. The mechanical properties of the degraded PCL were measured using a dynamic mechanical analyzer (DMA, Model Q850, TA Instruments, New Castle, DE, USA), as presented in Fig. 1(c). All samples were uniaxially stretched with a strain rate of 0.2 % s^{-1}.

2.2 Experimental results

Fig. 2 presents the normalized mass variation of the PCL strips after immersing in enzyme solution for different immer-

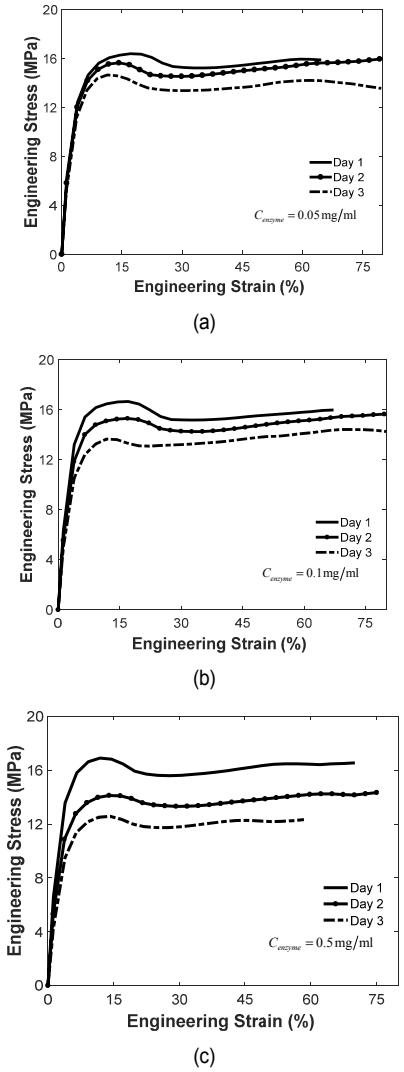

Fig. 3. The engineering strain-engineering stress of the PCL strips after immersing in enzyme solutions with different concentrations of (a) 0.05 mg/ml; (b) 0.1 mg/ml; (c) 0.5 mg/ml.

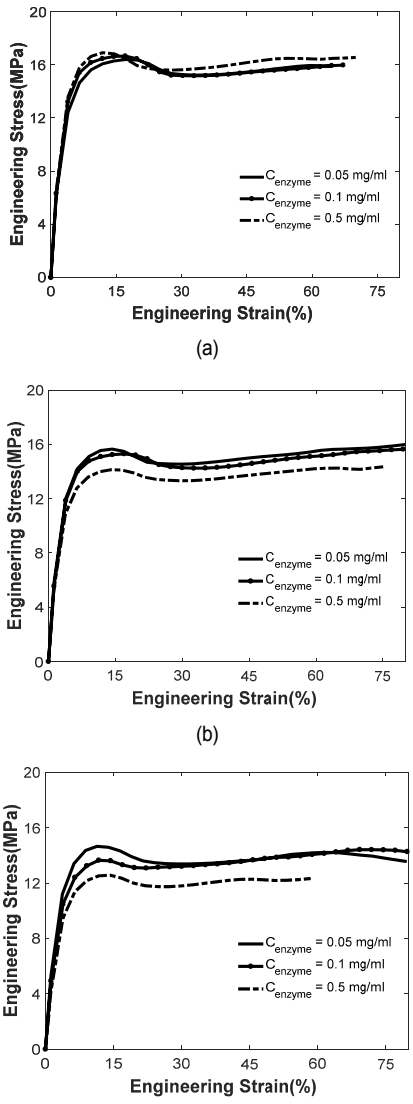

Fig. 4. The engineering strain-engineering stress of the PCL strips after immersing in enzyme solutions for different immersing times of (a) 1 day; (b) 2 days; (c) 3 days.

sion times. Total three enzyme concentration conditions are tested, i.e, 0.05 mg/ml, 0.1 mg/ml and 0.5 mg/ml. Quasi-linear weight decreases of the PCL sample are observed under enzyme degradation which suggests a non-Fickian diffusion properties of enzyme solution in the semicrystalline PCL. The weight decreases faster when the enzyme concentration is higher, which means a higher degradation rate of the crystals.

Fig. 3 plots the tested engineering stress-engineering strain of the degraded PCL strips after immersing in enzyme solutions for different times. The samples that immersed for a along time were difficult to be clamped in the DMA, therefore, only the samples immersed for three days were tested under three enzyme concentration conditions. It can be found from the figure that an obvious material softening takes place due to the plastic slips in the crystals. After the enzyme-degradation, the material strengths are decreased obviously. That is because that the enzyme solution diffuses into the PCL, decrystallizes the crystals and further cleaves the amorphous chains. When the enzyme concentration is higher, a more serious enzyme-activated degradation is induced in the PCL, leading to a larger material properties reduction, as plotted in Fig. 4, where the engineering stress-engineering strain relations of the degraded PCLs are presented under different enzyme concentration conditions.

3. Homogenization-based viscoplastic model for the semicrystalline PCL

3.1 General description

We aim to develop a homogenization-based viscoplastic model for the semicrystalline PCL featuring with the heat-

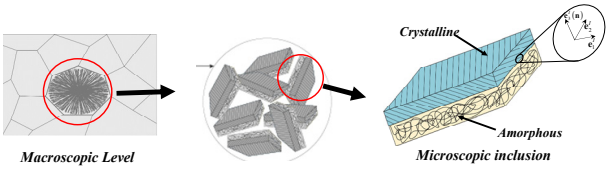

Fig. 5. (a) Schematic plot of multiscale structure of the semi-crystalline PCL; (b) in the microscopic level the spherulite consists of multi-laminated composite entities with different direction; (c) each composite entity consists of a crystal layer and an amorphous layer.

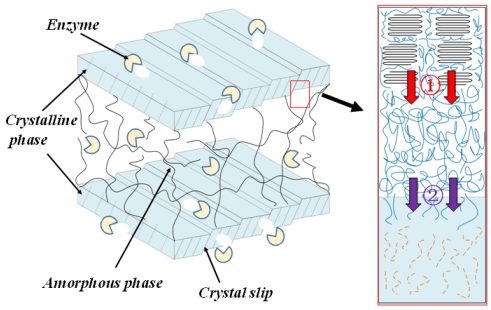

Fig. 6. Schematic plot of enzyme degradation of semi-crystalline PCL.

enzyme activated degradations. Following works [18, 20, 22-27], the semicrystalline PCL exhibits spherulitic morphologies with radial arrangements of broad thin crystalline lamellae infilled with amorphous layers, as plotted in Fig. 5(a). In the standard fashion of the multi-scale procedure, the overall properties of the PCL are extracted from nested representative volume elements (RVEs) containing an assemble of two-layer laminated composite inclusions with randomly distributed interface normal directions. Each inclusion comprises a crystalline lamella and amorphous lamella, as shown in Fig. 5(c).

Diffusants, such as ions and gas molecules, are difficult to permeate into the crystalline domains with tightly packed chains, as stated in the works [28, 29], which always cause a tortuous diffusion pathway along the boundary of crystals. Therefore, it is reasonably assumed that enzyme monomers mainly permeates into the amorphous domain, which results in a material swelling and the enzyme-activated cleavage of polymer chains. Simultaneously, crystals are decrystallized gradually on the crystal-amorphous interface, leading to an interface-front movement into the crystals. In the decrystallization area, the tightly aligned chains of crystals are unfolded and melt into the amorphous chains around, as schematic plotted in Fig. 6. Mainly two issues need to be settled in the process, i.e., (1) the enzyme-triggered decrystallization kinematics in addition to the thermally-activated melt mechanism; (2) the enzyme-triggered dissolution kinematics of amorphous chains.

In the following sections, the micromechanical model and the associated interaction law of composite inclusions are developed first. Then, the material models are developed for the crystal phase and the amorphous phase, respectively.

3.2 Micromechanical models for composite inclusion

3.2.1 Kinematical relations

(1) Deformation gradient

Denote the deformation gradient and enzyme concentration for each microscopic inclusion as $\mathbf{F}^I$, c^I, and the counterparts measured on each macro-material point as $\mathbf{F}$, and c. Through this work, all variables with superscript I indicate the variables defined for laminated inclusions, and that without superscript for the macro-material. Considering an aggregate of n inclusions at each macroscopic material point, we have the following deformation relation basing on the one-order homogenization algorithm

$$\mathbf{F} = \left\langle \mathbf{F}^{I_{(i)}} \right\rangle , \tag{1}$$

where the notation $\langle \bullet \rangle = \sum_{i=1}^{N} \chi^{I_{(i)}} (\bullet)^{I_{(i)}}$ denotes the operating algorithm for the volume average, and $\chi^{I_{(i)}}$ is the volume fraction of the i th inclusion. The superscript $I_{(i)}$ indicate that the variables are defined for the i th inclusion.

Basing on the generalized three-dimensional lamination theory, a piecewise uniform of deformation gradient within each phase is assumed, and the total deformation gradient of the laminated inclusion, $\mathbf{F}^I$, can be solved by a volume-weighted average of the crystalline layer and amorphous layer as

$$\mathbf{F}^{I_{(i)}} = f^{I_{(i)}^c} \mathbf{F}^{I_{(i)}^c} + (1 - f^{I_{(i)}^c}) \mathbf{F}^{I_{(i)}^a} , \tag{2}$$

where $f^{I_{(i)}^c}$ indicates the volume fraction of crystalline layer in the i th inclusion, and $\left(1 - f^{I_{(i)}^c}\right)$ for the amorphous layer; $\mathbf{F}^{I_{(i)}^c}$ and $\mathbf{F}^{I_{(i)}^a}$ are the deformation gradients for the amorphous layer and crystalline layer of the i th inclusion, respectively.

(2) Enzyme concentration

Since a large free volume and molecular disorder in amorphous layer, a significant rapid diffusive transport process was observed comparing to that in the tightly packed polymer crystalline domains [30]. Thus, we assume a uniform enzyme concentration distribution in amorphous layer in the considered time scale, $t \sim l^2 / D$ with l the characteristic length of RVE and D the diffusion coefficient. A gradual-decrystallization undergoes on crystal-amorphous interface resulting in a gradual transformation of crystals into amorphous, where areas behind the diffusion front in crystalline layer are reasonably assumed free of enzyme monomers, as plotted in the Fig. 6. Therefore, denoting the enzyme concentration in the i th laminates inclusion as $c^{I_{(i)}}$, and that at macromaterial point as c, we have the concentration relation of

$$c = \left\langle c^{I_{(i)}} \right\rangle = \left\langle \left(1 - f^{I_{(i)}^c}\right) c^{I_{(i)}^a} \right\rangle, \tag{3}$$

here $c^{I_{(i)}^a}$ are the enzyme concentrations in amorphous layer of the i th inclusion. Here all mass concentrations are defined as the mole numbers of enzyme monomers per unit volume.

For simplicity, we assume a same crystallinity for all inclusions at each macroscopic material point, i.e., $f^c = f^{I_{(i)}^c}$, $(i = 1,2,...,n)$. This assumption makes sense when the crystallinity is related only to the temperature and enzyme concentration, which are assumed uniform within all inclusions of each macroscopic point. By the way, it is not the case when the crystallinity is associated with the local stress and deformation, such as the discussed stretch-induced crystallization mechanisms in Ref. [31]. Upon above consideration, we have $c = \left(1 - f^c\right)\left\langle c^{I_{(i)}^a} \right\rangle$.

In this work, we aim to unveil underlying mechanisms in enzyme triggered dissolution of the PCL and the induced overall chemomechanical properties of the PCL with local microfeatures. At this point, the detailed descriptions of transient diffusion in local inclusion are omitted for a reasonable simple way to capture the complicated chemomechanical properties. Thus, a stable diffusion process is assumed in the RVE, which leads to a uniform distribution of the enzyme concentration, i.e., $c^{I_{(i)}} = c\ (i = 1,2,...,n)$.

(3) Inclusion interaction law

In each laminates inclusion, the interfacial compatibility and equilibrium conditions should be met according to the three dimensional lamination theory. Consider an inclusion with interface normal direction of $\mathbf{n}$, as plotted in Fig. 5(c). A local orthonormal vector basis $\mathbf{e}_i^I (i = 1,2,3)$ are set, with $\mathbf{e}_1^I$ and $\mathbf{e}_2^I$ the two unit vectors in the interface, and $\mathbf{e}_3^I = \mathbf{n}$ the unit normal vector of the interface with $\mathbf{e}_1^I \times \mathbf{e}_2^I = \mathbf{e}_3^I$. For later using, two fourth-order subspace projection tensors are defined as

$$\mathbb{P}_n^I = (\mathbf{I} - \mathbf{n}^I \otimes \mathbf{n}^I) \bar{\otimes} (\mathbf{I} - \mathbf{n}^I \otimes \mathbf{n}^I),\ \mathbb{P}_T^I = \mathbb{I} - \mathbb{P}_n^I, \tag{4}$$

here tensor operator $\bar{\otimes}$ is defined as $\left(\mathbf{A} \bar{\otimes} \mathbf{B}\right)_{ijkl} = A_{ik} B_{jl}$; $\mathbf{I}$ and $\mathbb{I}\left(\equiv \mathbf{I} \bar{\otimes} \mathbf{I}\right)$ are the second- and fourth-order identity tensors, respectively.

Then the strain tensors and the stress tensors of the inclusion, the crystalline layer and amorphous layer can be decomposed as

$$\begin{aligned} &\mathbf{E}^k = \mathbb{P}_T^I : \mathbf{E}^k + \mathbb{P}_n^I : \mathbf{E}^k, \\ &\mathbf{S}^k = \mathbb{P}_T^I : \mathbf{S}^k + \mathbb{P}_n^I : \mathbf{S}^k \ \ (k = I, I^a, I^c) \end{aligned} \tag{5}$$

Accordingly, the deformation continuous condition across interface of the inclusion can be written as

$$\mathbb{P}_T^I : \mathbf{E}^{I^c} = \mathbb{P}_T^I : \mathbf{E}^{I^a} = \mathbb{P}_T^I : \mathbf{E}^I, \tag{6}$$

and the stress continuous conditions of

$$\mathbb{P}_n^I : \mathbf{S}^{I^a} = \mathbb{P}_n^I : \mathbf{S}^{I^a} = \mathbb{P}_n^I : \mathbf{S}^I. \tag{7}$$

3.2.2 Free energy function and material solving

Denote the Helmholtz free energy density, measured as per unit initial volume, for the i th inclusion as $\psi^{I_{(i)}}\left(\mathbf{F}^{I_{(i)}}, c^{I_{(i)}}\right)$. Then the free energy density at each macroscopic material point of the PCL can be obtained by the Hill-Mandel principle as

$$\psi(\mathbf{F}, c) = \left\langle \psi^{I_{(i)}}\left(\mathbf{F}^{I_{(i)}}, c^{I_{(i)}}\right) \right\rangle. \tag{8}$$

Here the free energy density of the i th inclusion, $\psi^{I_{(i)}}\left(\mathbf{F}^{I_{(i)}}, c^{I_{(i)}}\right)$, is solved as inclusion-average over that of crystalline fraction and amorphous fraction as

$$\psi^{I_{(i)}} = f^c \psi^{I_{(i)}^c} + (1 - f^c)\psi^{I_{(i)}^a}, \tag{9}$$

where $\psi^{I_{(i)}^c}$ and $\psi^{I_{(i)}^a}$ are the defined free energy densities of the crystalline phase and amorphous phase of the i th laminates inclusion , respectively.

From a standard two-scale solving procedure, the following stress relation can be solved

$$\boldsymbol{\sigma} = \left\langle \boldsymbol{\sigma}^{I_{(i)}}\left(\mathbf{F}^{I_{(i)}}, c^{I_{(i)}}\right) \right\rangle, \tag{10}$$

where $\boldsymbol{\sigma}^{I_{(i)}}$ the Cauchy stress of the i th inclusion and $\boldsymbol{\sigma}$ is the volume-averaged Cauchy stress on macroscopic scale.

3.3 Constitutive relations of single inclusion

3.3.1 Crystalline phase

(1) Elasticity

To characterize the plastic slips in the crystalline phase, we multiplicatively decompose the mechanical deformation gradient $\mathbf{F}^{I^c}$ into the elastic part $\left(\mathbf{F}^{I^{ce}}\right)$ and plastic part $\left(\mathbf{F}^{I^{cp}}\right)$ as

$$\mathbf{F}^{I^c} = \mathbf{F}^{I^{ce}} \cdot \mathbf{F}^{I^{cp}}. \tag{11}$$

The following logarithm elastic strain measure and the plastic velocity gradient are defined as

$$\begin{aligned} &\mathbf{E}^{I^{ce}} = \ln\left(\mathbf{U}^{I^{ce}}\right),\ \ \mathbf{U}^{I^{ce}} = \left(\left(\mathbf{F}^{I^{ce}}\right)^T \cdot \mathbf{F}^{I^{ce}}\right)^{1/2}, \\ &\mathbf{D}^{I^{cp}} = sym\left(\dot{\mathbf{F}}^{I^{cp}} \cdot \left(\mathbf{F}^{I^{cp}}\right)^{-1}\right). \end{aligned} \tag{12}$$

It is well-known that the elastic properties of crystalline material depend on the crystallographic direction and crystallographic slip within slip systems [18, 20, 32]. Thus, we relate the

Mandel stress to the logarithm elastic strain by an anisotropic forth-order elastic modulus tensor, $\mathbb{L}^{I^c}$ as

$$\bar{\mathbf{M}}^{I^c} = \mathbb{L}^{I^c} : \mathbf{E}^{I^{ce}} . \tag{13}$$

For later use, we define the second Piola-Kirchhoff stress defined in initial configuration as

$$\begin{aligned} \mathbf{S}^{I^c} = & \left(\left(\mathbf{F}^{I^{cp}} \right)^{-1} \bar{\otimes} \left(\mathbf{F}^{I^{cp}} \right)^{-1} \right) : \bar{\mathbf{S}}^{I^c} = \\ & \left(\left(\mathbf{F}^{I^{cp}} \right)^{-1} \bar{\otimes} \left(\mathbf{F}^{I^{cp}} \right)^{-1} \right) : \left(\bar{\mathbf{C}}^{I^{ce}} \cdot \bar{\mathbf{M}}^{I^c} \right) \end{aligned} . \tag{14}$$

(2) Viscoplasticity

Following the works [18, 20, 32], the irreversible plastic strain rate of the crystalline phase is solved as a summation of multi-slip systems as

$$\bar{\mathbf{D}}^{I^{cp}} = \sum_{\alpha=1}^{K} \left(\dot{\gamma}^{\alpha} \mathbf{R}^{\alpha} \right) . \tag{15}$$

Here $\dot{\gamma}^{\alpha}$ is the shear strain rate of the α th slip system; $\mathbf{R}^{\alpha}$ is the Schmid's tensor of each crystallographic slip system, as

$$\mathbf{R}^{\alpha} = \frac{1}{2} \left(\mathbf{s}^{\alpha} \otimes \mathbf{n}^{\alpha} + \mathbf{n}^{\alpha} \otimes \mathbf{s}^{\alpha} \right) \ \text{(no sum)}, \tag{16}$$

with $\mathbf{s}^{\alpha}$ and $\mathbf{n}^{\alpha}$ are the slip direction and normal direction of the slip plane, respectively.

For each slip system, the shear rate $\dot{\gamma}^{\alpha}$ is defined as the power law function of its effective stress tensor $\tau^{I^{c(\alpha)}}$, according to the work by Miche et al. [33], as

$$\dot{\gamma}^{\alpha} = \dot{\gamma}_0^{\alpha} \frac{\tau^{I^{c(\alpha)}}}{G^{\alpha}} \left| \frac{\tau^{I^{c(\alpha)}}}{G^{\alpha}} \right|^{n_c - 1} , \tag{17}$$

where n_c is the rate exponent; $\dot{\gamma}_0^{\alpha}$ is the reference strain rate and G^{α} the strength of the α th slip system. Here the reference strain rate are set same for all slip systems for simplicity consideration. The effective driven force is solved as $\tau^{I^{c(\alpha)}} = \left(\mathbf{M}^{I^c} : \mathbb{D} \right) : \mathbf{R}^{\alpha}$, with $\mathbb{D} (\equiv \mathbb{I} - \mathbf{I} \otimes \mathbf{I}/3)$ the deviatoric projection tensor; $\mathbb{I}$ and $\mathbf{I}$ are the forth and second order identity tensor, respectively. Since the thickness of the crystalline laminates is small, and the plastic strengthening is neglected as done in the work [20].

(3) Texture evolution

To capture the crystallographic axes' variation, we decompose the spin tensor $\mathbf{W}^c$ into the plastic spin $\mathbf{W}^p$ and lattice spin $\mathbf{W}^*$, and the lattice spin of each inclusion is solved as [20]

$$\mathbf{W}^{I^*} = \mathbf{W}^{I^c} - \sum_{\alpha}^{K} \dot{\gamma}^{\alpha} \mathbf{A}^{\alpha} . \tag{18}$$

where $\mathbf{A}^{\alpha}$ is the skew part of the Schmid tensor of slip system α, defined as $\mathbf{A}^{\alpha} = \left(\mathbf{s}^{\alpha} \otimes \mathbf{n}^{\alpha} - \mathbf{n}^{\alpha} \otimes \mathbf{s}^{\alpha} \right) / 2$. $\mathbf{W}^{I^c}$ is the skew part of the velocity gradient, defined as $\mathbf{W}^{I^c} = \left(\boldsymbol{l}^{I^c} - \left(\boldsymbol{l}^{I^c} \right)^T \right) / 2$. Then the crystallographic chain axis of the inclusion change with a rate of

$$\dot{\mathbf{n}}_c^I = \mathbf{W}^{I^*} \cdot \mathbf{n}_c^I . \tag{19}$$

Using the above equation, the crystallographic axe direction at time step $t + \Delta t$ can be solved in an incremental form over the time increment t to $t + \Delta t$, as $\mathbf{n}_c^I (t + \Delta t) = \exp \left(\Delta t \mathbf{W}^{I^*} \right) \cdot \mathbf{n}_c^I (t)$. Here $\mathbf{n}_c^I (t)$ is the solved crystallographic axe direction at time step t and the exponential function is solved using the Cayley-Hamilton theorem [20] as

$$\begin{aligned} \exp \left(\Delta t \mathbf{W}^{I^*} \right) = & \mathbf{I} + \frac{(\sin w)}{w} \left(\Delta t \mathbf{W}^{I^*} \right) \\ & + \left(\frac{1 - \cos w}{w^2} \right) \left(\Delta t \mathbf{W}^{I^*} \right)^2 \end{aligned} , \tag{20}$$

with $w^2 = -\mathrm{tr} \left[\left(\Delta t \mathbf{W}^{I^*} \right)^2 \right] / 2$.

(4) Crystallization/melt under chemical and temperature activation

The enzyme-activated decrystallization have been researched in some works, and the decrystallization rate was generally considered to be proportional to the chemical solution concentration [21] the crystal size and the crystal amounts [21, 28]. Also, the thermally-activated melt-crystallization behaviors have been well explored in Ref. [34]. Accordingly, the following evolution rate of crystals is proposed, which is assumed to be related to the solution concentration, the fraction of crystals and the temperature,

$$\dot{f}^{I^c} = -k_c (T, c) f^{I^c} H \left(f^{I^c} \right) , \tag{21}$$

where f^{I^c} is the crystalline fraction of the inclusion. $k_c (T, c)$ is the decrystallization rate constant related to the temperature and enzyme concentration. $H \left(f^{I^c} \right)$ is the Heaviside step function,

$$H \left(f^{I^c} \right) = \begin{cases} 0 & f^{I^c} < 0 \\ 1 & f^{I^c} \geq 0 \end{cases} . \tag{22}$$

The decrystallization rate is supposed to depend on both en-

zyme concentration and temperature. We decouple these two effects for simple consideration, i.e.

$$k_c(T,c) = k_{eg}(c)k_T(T), \tag{23}$$

where $k_{eg}(c)$ is enzyme concentration dependent decrystallization rate, and $k_T(T)$ is temperature dependent. In our parallel work [35], we have developed the enzyme-activated decrystallization rate of semicrystalline polymer under thermodynamic framework as

$$k_c(T,t) = G_0 \exp\left\{-\frac{E_a}{R\left[T(t)-T_\infty\right]}\right\}\exp\left[-\frac{K_g}{T(t)\Delta Tf}\right], \tag{24}$$

where G_0 is the reference rate, E_a and K_g the activation energy, $T(t)$ the temperature, R the gas constant, T_∞ the reference temperature constant. f is the induced corrector factor,

$$f = \frac{2T}{\left(T+T_m^0\right)}, \tag{25}$$

where T_m^0 is the melting reference temperature.

3.3.2 Amorphous phase

For theoretical derivation convenience, the deformation gradient of amorphous layer is multiplicatively separated into a mechanical part, $\mathbf{F}^{I_{(i)}^{am}}$, and a swelling part,

$$\mathbf{F}^{I_{(i)}^{as}}, \mathbf{F}^{I^a} = \mathbf{F}^{I^{am}} \cdot \mathbf{F}^{I^{as}}, \tag{26}$$

where $\mathbf{F}^{I_{(i)}^{as}} = J^s\mathbf{I}$, and J^s is the swelling volume, which is assumed entirely due to the fluid content change as

$$J^s = 1 + \upsilon\frac{c}{\left(1-f^c\right)}, \tag{27}$$

where υ indicates the mole volume of enzyme solution. Here we have used relation of $c^{I^a} = c^a/(1-f^c)$, with c^a the number concentration of enzyme molecules permeated in the amorphous layer, measured as mole number per volume in initial configuration.

The amorphous phase in each considered inclusion, composed of randomly coiled macromolecules, is often regarded incompressible. To make current model more general, the generalized neo-Hookean model with volume expansion is applied as

$$\psi^{I^a} = N_a k_b T\left(\overline{I}_1^{I^a} - 3\right) + \frac{1}{2}J^s K \ln\left(J_m^{I^a}\right)^2, \tag{28}$$

here T is temperature and k_b the Boltzmann constant. $\overline{I}_1^{I_{(i)}^a}$ is the first invariant of the strain tensor, i.e., $\overline{I}_1^{I_{(i)}^a} = \mathrm{tr}\left(\det(\mathbf{C}^{I_{(i)}^{am}})^{-1/3}\mathbf{C}^{I_{(i)}^{am}}\right)$ with $\mathbf{C}^{I_{(i)}^{am}} = \left(\mathbf{F}^{I_{(i)}^{am}}\right)^T \cdot \mathbf{F}^{I_{(i)}^{am}}$, and the volume deformation $J_m^{I_{(i)}^a} = \det\left(\mathbf{F}^{I_{(i)}^{am}}\right)$. J^s is the swelling volume defined in Eq. (27).

The crosslinking chain density N_a (Eq. (28)), which is degraded gradually under enzyme activated dissolution. The enzyme-triggered dissolution rate of the crosslinked concentration has been developed in our previous work [35] as

$$\dot{N}_a = -K_{c0}\exp\left(-\frac{E_a}{RT}\right)cN_a. \tag{29}$$

Solving of the above evolution equation with initial conditions for c and N_a, yields the crosslinked chains density, which is used in Eq. (28).

Thus the stress of the amorphous layer can be solved by Eq. (28) as

$$\begin{aligned}\mathbf{S}^{I^a} = 2\frac{\partial\psi^{I^a}}{\partial\mathbf{C}} = 2Nk_bT\left(J^{-2/3}\left(\mathbb{I}-\frac{1}{3}\mathbf{C}\otimes\mathbf{C}^{-1}\right):\mathbf{I}\right),\\ +2\left(J^sK\ln\left(J_m\right)\mathbf{C}^{-1}\right)\end{aligned} \tag{30}$$

with $\mathbf{S}^{I^a}$ the second Piola-Kirchhoff stress.

Applying the Eqs. (14) and (30) and using Eq. (10), we have the total stress of the PCL as

$$\mathbf{S} = f^c\left\langle\mathbf{S}_{PCL}^{I^c}\right\rangle + \left(1-f^c\right)\left\langle\mathbf{S}_{PCL}^{I^a}\right\rangle. \tag{31}$$

Assume the free energy change due to permeation of enzyme solution is captured by following formation of mixing energy,

$$\rho_R\psi^{mix} = \frac{RT}{\upsilon}\left(\upsilon c\log\left(1+\frac{1}{\upsilon c}\right)+\frac{\chi}{1+\upsilon c}\right). \tag{32}$$

Considering the Eq. (28), the chemical potential can be solved as

$$\begin{aligned}\mu = \mu_0 + RT\left(\ln\left(\frac{\upsilon c}{1+\upsilon c}\right)+\frac{1}{1+\upsilon c}+\chi\frac{1}{\left(1+\upsilon c\right)^2}\right).\\ -\left(1-f^c\right)K\upsilon\ln\left(J_m\right)^2+\frac{\left(1-f^c\right)}{2}K\upsilon\ln\left(J_m\right)^2\end{aligned} \tag{33}$$

with μ_0 the reference chemical potential.

3.4 Non-Fickian diffusion equation

The enzyme concentration distribution in the PCL can be ob-

tained by solving the following local mass diffusion equation, derived from mass conservation law [36]

$$\dot{c} = -\nabla \cdot \boldsymbol{j}_E \,. \tag{34}$$

Here, $\boldsymbol{j}_E$ is the mass flux, which is often assumed to obey a 'Darcy-type' relation [36, 37], i.e., a linear dependence of the mass flux $\boldsymbol{j}_E$ on the chemical potential gradient $\nabla \otimes \mu$,

$$\boldsymbol{j}_E = -\mathbf{m} \cdot (\nabla \otimes \mu) \text{, and } \mathbf{m} = \frac{\mathbf{D}c}{RT} \,, \tag{35}$$

here c is the mass concentration, R and T are gas constant and temperature, μ is the chemical potential. $\mathbf{D}$ is the diffusion coefficient tensor, and set as $\mathbf{D} = D\mathbf{I}$ for an isotropic diffusion.

From experimental results in Sec. 2.2.1, a general case II diffusion behaviors is observed. However, the above constitutive relation is inconvenient for description of case II diffusion where a sharp diffusion front is observed, though it has been successfully applied in some models by considering the dependence of diffusion coefficient D on local mass concentration. For example, to solve the Li ion diffusion in the electrode, Yang et al. [38] assumed a fast diffusion coefficient when the concentration fraction is larger than 0.1, while $D \to 0$ when the concentration fraction is less than 0.1. This procedure always results in convergence problem when applied with finite element method. In another work, a complex model was developed based on free volume theory to capture the lagging behavior by the plasticization effect [36]. However, this model is limited in capture the diffusion sluggish due to more effects, such as chemical reaction, species blocked effect, and etc. Tzou [39] developed a dual-phase-lag model to solve the wave-like heat conduction when under rapid heating, which was demonstrated later effective to capture the lag in mass diffusion process. The mass diffusion in the semi-crystalline PCL is hindered by interactions of enzyme monomers with the crystals in process of decrystallization and the de-bonding of the polymer chains within the material. These molecular effects are supposed to cause a lagging response in the diffusion behavior, which is within the context of the dual-phase-lag approach. By introducing two lag parameters to depict the sluggish effect following the dual-phase-lag model [39, 40], the mass flux is defined as

$$\boldsymbol{j}_E\left(\mathbf{x}, t + \tau_j\right) = -\mathbf{m} \cdot \left(\nabla \otimes \mu_E\left(\mathbf{x}, t + \tau_c\right)\right) \,. \tag{36}$$

Here τ_j and τ_c are two introduced retardation times, to reflect the delay in formation of the concentration gradient and the flux. Taking the first order Taylor expansion with respect to time, and applying the mass balance of the diffusion species, the following quasi-hyperbolic diffusion law can be obtained as

$$\frac{1}{J}\left(\dot{c} + \tau_j \ddot{c}\right) = \nabla \cdot \left(\mathbf{m} \cdot \left(\nabla \otimes \mu\right)\right) + \tau_c \nabla \cdot \left(\mathbf{m} \cdot \left(\nabla \otimes \dot{\mu}\right)\right) \,. \tag{37}$$

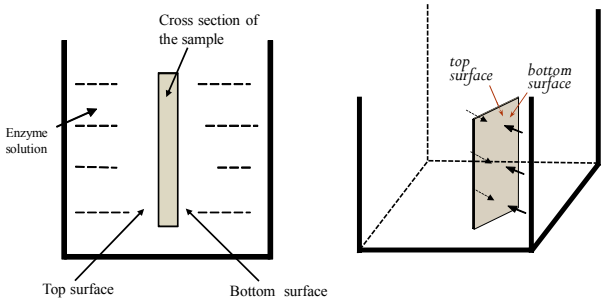

Fig. 7. Schematic plot of the PCL samples that immersing in the enzyme solutions.

As the τ_j and τ_c equal zero, the above equation is transformed to the general diffusion model [37].

4. Model results and discussions

The developed 3D constitutive model is solved by coding with MATLAB. The enzyme diffusion of Eq. (37) is solved by finite difference method, which is detailed in Appendix A.1. Using the constitutive relations (Eqs. (13) and (30)) and compatible conditions (Eqs. (6) and (7)), a convergent result is sought for each inclusion by applying the self-consistent model for large deformation provided in the work [20]. Then, the overall chemomechanical properties of the PCL are solved by volume averaged procedure. The solving method for uniaxial loading of the PCL follows the procedure in our previous work [41], and presented in details in Appendix A.2. Here, a total of 240 inclusions are solved at each material point.

In the following, the model is calibrated by the related experimental results first, and then applied for the chemomechanical properties of the PCL. The local crystallography axe variations under large stretch have also been discussed when degraded under enzyme solution. The identified material parameters are listed in Tables 1 and 2. Here total 5 model parameters regarding thermomechanical of PCL are fitted by the engineering stress-engineering strain curves. The other 4 model parameters associated with enzyme degradation are cited from the work [41].

4.1 Degradation of the PCL

4.1.1 Enzyme diffusion

The enzyme diffusion in PCL is simulated and discussed in this section. According the immersion experiment (Fig. 1), enzyme mainly permeated in from the bottom and top surfaces of the sheet sample, with in-plane size of ~12 mm and thickness of ~0.47. Thus, a 1D diffusion case is reasonably simplified, as schematic plot in Fig. 7 In the simulation, two end boundaries are set as concentration condition of $c_{x=0} = c_{x=l} = 1$. The finite difference method is applied and 100 discrete points are discreted along the thickness. A detailed solving method is presented in the Appendix A.1. The fitted retardation times are

Table 1. Material parameters for the enzyme diffusion and enzyme-activated decrystallization of the PCL.

Parameter	Values	Description	
K_{eg}^{0}	1.2×10^{-3}	Reference decrystallization rate	Fitted
K_{c0}	1.2×10^{-2}	Reference reaction constant	Fitted
E_a	1×10^{3} J	Activation energy of the reaction	Fitted
D	1.0×10^{-10} m^2/s	Diffusion coefficient	Fitted

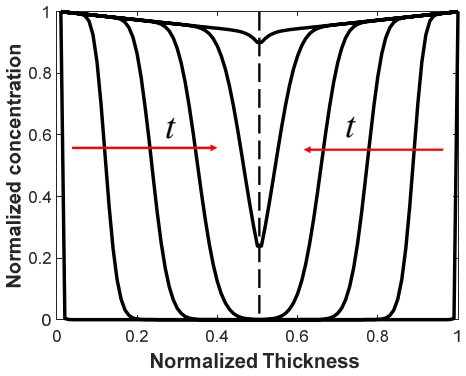

Fig. 8. Normalized concentration distribution along the thickness for different diffusion time. The red arrow indicates the time increase direction.

$\tau_j = 1\times10^3$ s and $\tau_c = 1\times10^2$ s, and the diffusion coefficient is fitted as $D = 1.0\times10^{-10}$ m^2/s, as listed in Table 1. Fig. 8 presents the concentration profile along the thickness of the sample along with immersion time. A sharp advancing interface can be found between the inner glassy core without any enzyme and the outer swollen area swollen by the permeated enzyme solution. An equilibrium or nearly equilibrium concentration of the sorbate is achieved behind the advancing front, while the area ahead has no diffusion take place. From the figure it can be found current model predict a general case II diffusion behaviors. The related mass variations of the degraded PCLs are discussed in the following section.

4.1.2 Enzyme triggered dissolution of the PCL

Fig. 9 presented variation of the simulated normalized mass of EDSMC, and the experimental result are also plotted for comparison. Here the degradation of the PCL is solved at room temperature (25 °C), and three enzyme concentrations (0.05, 0.1 and 0.5 mg/mL), are considered. From the figure, it can be found that the simulated mass variations agree generally well with the experimental results along with immersion time. When the concentration is higher, a quicker dissolution of the semicrystalline PCL is observed. The PCL sample has nearly been dissolved completely after ~6 days immersing in the enzyme solution of 0.5 mg/ml.

Fig. 10 presents the crystallinity of the semi-crystalline polymer when immersed in enzyme concentration, as well as the volume fractions of the amorphous phase and the dissolved segments. A gradual decease of the crystal fraction and amorphous phase can be observed as enzyme permeated in as immersion time increases. When the enzyme concentration is higher, the degradation rate of the polymer is faster, where the higher enzyme concentration induces a fast decrystallization rate and the dissolution rate. It is found only ~6 days is needed to completely dissolute the sample when under 0.5 mg/ml enzyme solution. It is interesting to observe that the fraction of the amorphous depends on the “competition mechanism” between the dissolution rate of amorphous chains and decrystallization

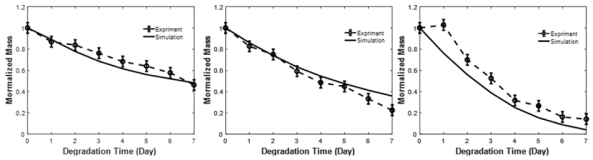

(a) (b) (c)

Fig. 9. Variation of the normalized mass of PCL-composite along with immersion time.

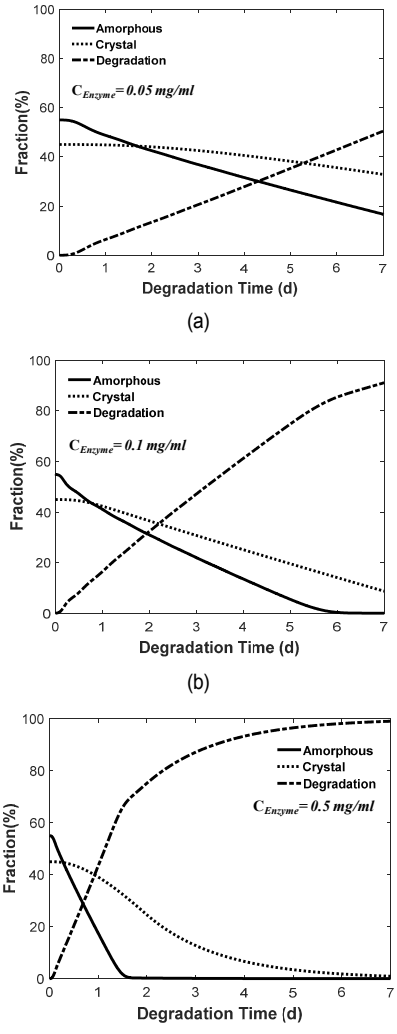

(a) (b) (c)

Fig. 10. Variation of the fractions of the crystals, the amorphous and the cleavaged segments along with immersion time.

Table 2. Mechanical parameters of the PCL.

Parameter	Values	Description	
N_a	1×10^{25} mol/m^3	Crosslinking density of amorphous phase	Fitted
μ	400 MPa	Shear modulus	Fitted
K	1 GPa	Bulk modulus	Fitted
G^c	20 MPa	Initial yield strength	Fitted
$\dot{\gamma}_0^c$	0.001	Reference plastic strain rate	Fitted

Table 3. Slip systems of the PCL and the normalized resistances.

	Slip sysem	G^a / G^c
Chain slips	(100)[001]	1.0
	(010)[001]	2.5
	(110)[001]	2.5
	(1$\bar{1}$0)[001]	2.5
Transverse slips	(100)[001]	1.66
	(010)[100]	2.5
	(110)[1$\bar{1}$0]	2.2
	($\bar{1}$10)[110]	2.2

rate of crystals, because the polymer chains decrystallized from the PCL would mix into the swelling amorphous area, and further increase the amorphous fraction.

4.2 Viscoplastic behavior of the EDSMC

In this section, the viscoplastic mechanical properties of the PCL are simulated with the developed homogenization-based model. Fig. 11 plots the simulated engineering stress-engineering strain under uniaxial stretch, and compared with the experimental results. Here the stress is solved by averaging over all finite difference points along the sample thickness, as done in the work [42]. The stretch rate is set as 0.2 % s-1 according to the experimental sets. The detailed parameter calibration is presented in the Appendix A.3, and the identified material parameters are listed in Table 2. Here the anisotropic elastic matrix of the crystalline phase is set as [43]

$$E_c = \mu \begin{bmatrix} 1 & 0.5 & 0.5 & 0 & 0 & 0 \\ 0.5 & 1 & 0.5 & 0 & 0 & 0 \\ 0.5 & 0.5 & 30 & 0 & 0 & 0 \\ 0 & 0 & 0 & 0.5 & 0 & 0 \\ 0 & 0 & 0 & 0 & 0.5 & 0 \\ 0 & 0 & 0 & 0 & 0 & 0.5 \end{bmatrix},$$

and the μ is fitted by the experiments as 400 MPa, as listed in Table 2.

Here a number of 240 inclusions are simulated at each macroscopic material point for the PCL. Total 8 slip systems are considered for each crystal, and the slip resistances are set according to the work [20], and shown in Table 3. The reference yield strength G^c is fitted by experiment as 20 MPa and listed in Table 2.

It can be found from the Fig. 11 that the PCL has a yield strength of ~16 MPa after immersed in enzyme concentration for 1 day, and then exhibits an obvious soften behavior due to crystal slips followed with a stress platform, where mainly amorphous fraction contributes. Both of the material modulus and yield strength decrease obviously along with the immersion time increases due to the enzyme-triggered decrystallization and dissolution, as discussed in Sec. 4.1. From the figures it can be found current model capture well the chemomechanical properties of the PCL when under enzyme degradation for different enzyme conditions. As for the case of immersing in 0.5 mg/ml for 3 days, there is a nearly ~10 % error between the simulations and experimental results, which maybe due to the numerical errors.

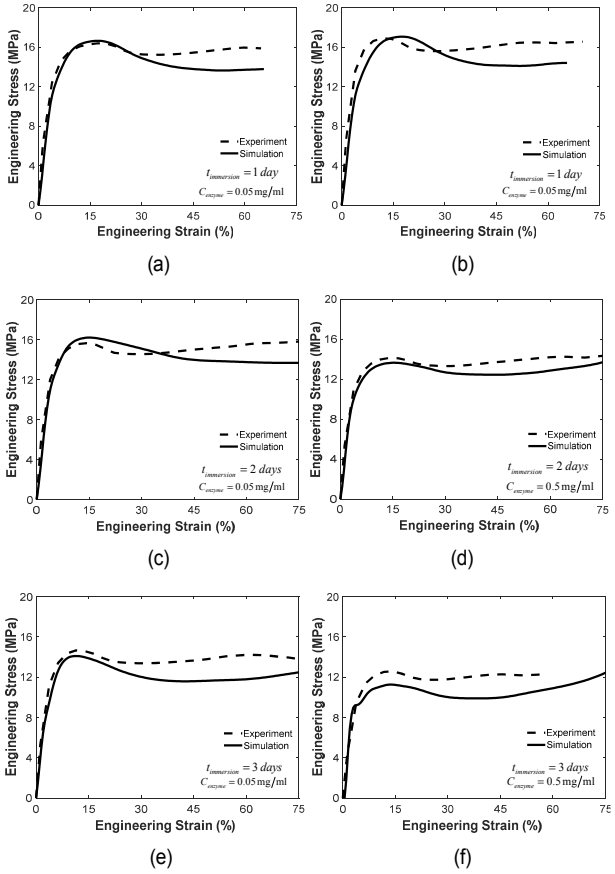

Fig. 11. The simulated engineering stress-engineering strain of the enzyme-degraded PCL and compared with experiment results.

4.2.1 Texture evolution

The effects of the enzyme-degradation on the crystallography axe direction are discussed in this section by applying the developed model, aiming to get a deep understanding in the chemomechanical properties of the PCL. The pole figures of the randomly-generated 240 inclusions are plotted in equal

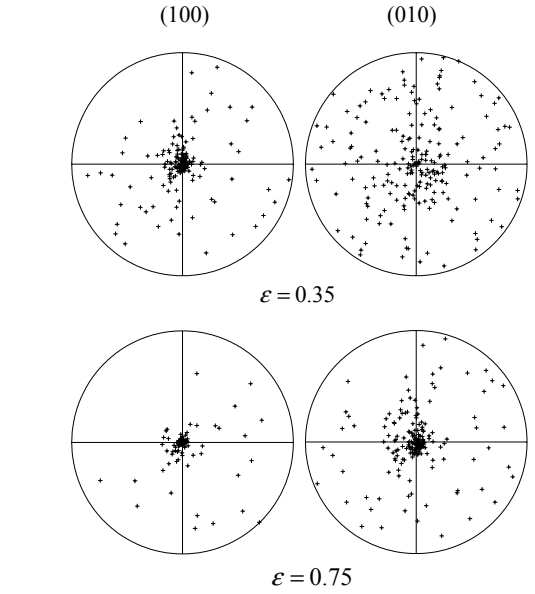

Fig. 12. Equal area projection pole figures of the slip systems of (100)[001] and (010)[001] when under different stretched strain.

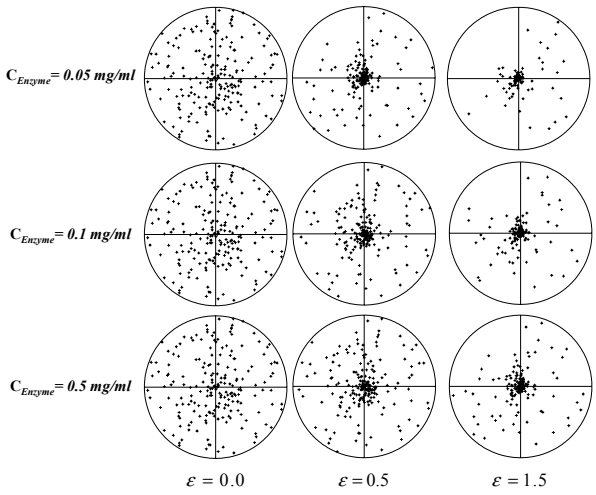

Fig. 13. Equal area projection pole figures of the crystallographic texture of the enzyme-degraded PCL for different stretched strain.

area projection in the Fig. 12, where two slip systems (100)[001] and (010)[001] are plotted for different strain. It can be observed from the figure that the (100)[001] is more easy to be active. When the engineering strain is $\varepsilon = 035$, the slip systems(100) are moving towards the stretch direction, while the slip systems (010) are still in nearly isotropic distribution. As stretch increases, the slip systems (010) become active and are moving towards to the stretch direction. That is because the slip systems (100)[001] have a lower yield strength than that of the slip systems (010)[001], as listed in the Table 3. What is more, it is easy to find that a high anisotropic property will be induced for the initially isotropic semicrystalline PCL when the inclusions rotate greatly under large stretch, as discussed in Ref. [20]. In this work, we mainly discuss the enzyme-degraded uniaxial stretch properties of the PCL, and a more detailed discussions on the stretch-induced anisotropic properties of the PCL can be rereferred to our parallel work [35].

The crystallography axe directions of the inclusions are plotted in equal area projection in Fig. 13 for different stretches after immersing in enzyme solutions for 7 days. Here three enzyme concentration solutions are considered as c_{enzyme} = 0.05 mg/ml, 0.1 mg/ml and c_{enzyme} = 0.5 mg/ml, respectively. It can be observed form the figure that the initially isotropic distributed crystallographic axe directions of the PCL migrate toward the stretch direction as stretches increase. The predicted patterns of crystallographic and morphological texture depends on the enzyme concentration. After immersing in enzyme solution for some times, the direction migrations of the crystallographic axes are less than the case where no enzyme degradation takes place. That is because the slips resistances within crystals are lowered under enzyme degradation, as observed in the Fig. 11, which result in great plastic slips and plastic spins within the crystals. Thus, the higher of the enzyme concentration conditions, a smaller migration of the crystallographic axes is obtained. The enzyme degradation relax the stretch-induced anisotropic properties of the PCL.

5. Conclusion

A 3D finite deformation viscoplastic model is developed for Poly(ε-caprolactone) (PCL) when under enzyme degradation. The degradation properties of the PCL under enzyme activation are investigated, and accordingly the overall chemomechanical properties of PCL-composite are discussed. Through volume average of a collects of laminated inclusions with crystals, the overall viscoplastic properties of PCL are solved by the homogenization-based procedure. The model is calibrated by related experiments, and then applied to explore the dissolution properties and chemomechanical properties of the PCL when under enzyme activation. Due to the enzyme-activated decrystallization and dissolution, the material stiffness and yield strengths of the semicrystalline PCL are decreased gradually. Simulation results show that the crystallographic axes of the PCL mitigate as the stretch increases. When consider enzyme-activated dissolution, the mitigations of the crystallographic axes become smaller which relax the stretch-induced anisotropic properties of the PCL. The research in this work provides theoretical foundation for the design and application of the PCL and PCL-composite.

Acknowledgments

The authors would like to acknowledge with great gratitude for the supports of the National Science Foundation of China (Grant No: 11772124), the Science Foundation of Hunan Province (Grant No: 2018JJ3027) and National Science Foundation of China for Outstanding Youth (Grant No: 11922206).

Nomenclature

$\mathbf{F}^{I}$: The deformation gradient for each microscopic inclusion
c^{I} : The enzyme concentration for each microscopic inclusion
$\chi^{I_{(i)}}$: The volume fraction of the i th inclusion
$I_{(i)}$: The enzyme concentration for each microscopic inclusion
$f^{I^{c}_{(i)}}$: The volume fraction of crystalline layer in the i th inclusion
$\mathbf{F}^{I^{c}}$: The deformation gradients for the crystalline layer
$\mathbf{F}^{I^{c}_{(i)}}$: The deformation gradients for the crystalline layer of the i th inclusion
$\mathbf{F}^{I^{a}_{(i)}}$: The deformation gradients for the amorphous layer of the i th inclusion
l : The characteristic length of RVE
D : The diffusion coefficient
$c^{I_{(i)}}$: The enzyme concentration in the i th laminates inclusion
$c^{I^{a}_{(i)}}$: The enzyme concentrations in amorphous layer of the i th inclusion
$\psi^{I_{(i)}}$: The Helmholtz free energy density, measured as per unit initial volume, for the i th inclusion
$\boldsymbol{\sigma}^{I_{(i)}}$: The Cauchy stress of the i th inclusion
$\boldsymbol{\sigma}$: The volume-averaged Cauchy stress on macroscopic scale
$\mathbf{E}^{k}$: The strain tensors of the inclusion
$\mathbf{S}^{k}$: The stress tensors of the inclusion
$\mathbf{F}^{I^{ce}}$: The elastic part of the mechanical deformation gradient $\mathbf{F}^{I^{c}}$
$\mathbf{F}^{I^{cp}}$: The plastic part of the mechanical deformation gradient $\mathbf{F}^{I^{c}}$
$\bar{\mathbf{M}}^{I^{c}}$: The Mandel stress to the logarithm elastic strain for the crystalline layer
$\mathbf{S}^{I^{c}}$: The second Piola-Kirchhoff stress defined in initial configuration for the crystalline layer
$\bar{\mathbf{D}}^{I^{cp}}$: The irreversible plastic strain rate of the crystalline phase
$\dot{\gamma}^{\alpha}$: The shear strain rate of the α th slip system
$\mathbf{R}^{\alpha}$: The Schmid's tensor of each crystallographic slip system
$\mathbf{s}^{\alpha}$: The slip direction
$\mathbf{n}^{\alpha}$: The normal direction of the slip plane
$\tau^{I^{c}(\alpha)}$: The effective stress tensor of the shear rate $\dot{\gamma}^{\alpha}$
n_{c} : The rate exponent
G^{α} : The strength of the α th slip system
$\dot{\gamma}_{0}^{\alpha}$: The reference strain rate
$\mathbf{W}^{I^{*}}$: The lattice spin of each inclusion
$\mathbf{W}^{I^{c}}$: The skew part of the velocity gradient
$\mathbf{A}^{\alpha}$: The skew part of the Schmid tensor of slip system α
$\dot{\mathbf{n}}_{c}^{I}$: The rate of the change for the crystallographic chain axis of the inclusion
$\dot{f}^{I^{c}}$: The evolution rate of crystals
k_{c} : The decrystallization rate constant related to the temperature and enzyme concentration
H : The Heaviside step function
k_{eg} : The decrystallization rate for the decrystallization of semicrystalline polymer
k_{eg}^{0} : The reference decrystallization rate which is to be fitted by the experiment
σ_{e} : The side surface free energy
Δh_{f} : The fusion heat
T_{m}^{0} : The melting temperature
k_{c} : The crystal/melt growth rate
G_{0} : The reference rate
T_{∞} : The reference temperature constant
E_{a}, K_{g} : The activation energy
R : The gas constant
f : The induced corrector factor
$\mathbf{F}^{I^{am}_{(i)}}$: The mechanical part of the deformation gradient of amorphous layer
$\mathbf{F}^{I^{as}_{(i)}}$: The swelling part of the deformation gradient of amorphous layer
J^{s} : The swelling volume
u : The mole volume of enzyme solution
$c^{I^{a}}$: The number concentration of enzyme molecules permeated in the amorphous layer of inclusion
c^{a} : The number concentration of enzyme molecules permeated in the amorphous layer
$\psi^{I^{a}}$: The Helmholtz free energy density, measured as per unit initial volume for the amorphous layer
N_{a} : The crosslinking chain density
$\bar{I}_{1}^{I^{a}_{(i)}}$: The first invariant of the strain tensor
$\mathbf{S}^{I^{a}}$: The stress of the amorphous layer, the second Piola-Kirchhoff stress
$\mathbf{S}$: The total stress of the PCL
$\rho_{R}\psi^{mix}$: Mixing energy
μ_{0} : The reference chemical potential
μ : The chemical potential
R_{i} : The reactants and products
ξ_{i} : The stoichiometry coefficients, measured in moles per volume
$\dot{c}_{\alpha}$: Changes of reactant/product concentrations
$\dot{\ell}_{c}$: The chemical reaction rate
E_{a} : The activation energy
c : The mole concentration of enzyme
N_{a} : The crosslinked network density per unit volume of the amorphous fraction
$\dot{N}_{a}$: The rate of change of the crosslinked network density of the amorphous fraction
$\boldsymbol{j}_{E}$: The mass flux
$\mathbf{D}$: The diffusion coefficient tensor
τ_{j}, τ_{c} : Retardation times
E_{c} : The anisotropic elastic matrix of the crystalline phase
μ : The shear modulus of the PCL
G^{c} : Initial yield strength
K : The bulk modulus of the PCL

References

[1] B. Feng et al., Engineering cartilage tissue based on cartilage-derived extracellular matrix cECM/PCL hybrid nanofibrous scaffolds, *Materials and Design,* 193 (2020) 108773.
[2] M. G. Gandolfi et al., Highly porous polycaprolactone scaffolds doped with calcium silicate and dicalcium phosphate dihydrate

designed for bone regeneration, *Materials Science and Engineering: C,* 102 (2019) 341-361.
[3] L. G. Griffith, Polymeric biomaterials, *Acta. Mater.*, 48 (2000) 263-277.
[4] K. P. Andriano et al., Technical note: biomechanical analysis of two absorbable fracture fixation pins after long-term canine implantation, *J. Biomed. Mater. Res. Part B*, 48 (1999) 528-533.
[5] S. L. Buffington et al., Enzymatically triggered shape memory polymers, *Acta Biomaterialia,* 84 (2019) 88-97.
[6] B. Narasimhan and S. K. Mallapragada, Dissolution of amorphous and semicrystalline polymers: mechanisms and novel applications, *Recent Res. Dev. Macromol Res.,* 3 (2) (1998) 1-24.
[7] W. H. Lee et al., Kinetics of solvent-induced crystallization of poly(ethylene terephthalate) at the final stage, *Journal of Polymer Research,* 10 (2) (2003) 133-137.
[8] H. Chen et al., Highly pH-sensitive polyurethane exhibiting shape memory and drug release, *Polymer Chemistry*, 5 (17) (2014) 5168.
[9] F. He, S. Li, M. Vert and R. Zhuo, Enzyme-catalyzed polymerization and degradation of copolymers prepared from ϵ-caprolactone and poly(ethylene glycol), *Polymer*, 44 (18) (2003) 5145-5151.
[10] M. F. Herman and S. F. Edwards, A reptation model for polymer dissolution, *Macromolecules,* 23 (15) (1990) 3662-3671.
[11] E. Kaunisto et al., A mechanistic modelling approach to polymer dissolution using magnetic resonance microimaging, *Journal of Controlled Release,* 147 (2) (2010) 232-241.
[12] B. A. MillerChou and J. L. Koenig, A review of polymer dissolution, *Progress in Polymer Science,* 28 (8) (2003) 1223-1270.
[13] B. Narasimhan and N. A. Peppas, The physics of polymer dissolution: modeling approaches and experimental behavior, *Polymer Analysis Polymer Physics. Advances in Polymer Science*, 128 (1997).
[14] S. K. Mallapragada and N. A. Peppas, Dissolution mechanism of semicrystalline poly(vinyl alcohol) in water, *Journal of Polymer Science, Part B: Polymer Physics,* 34 (7) (1996) 1339-1346.
[15] C. M. Hassan, J. H. Ward and N. A. Peppas, Modeling of crystal dissolution of poly(vinyl alcohol) gels produced by freezing/thawing processes, *Polymer,* 41 (18) (2000) 6729-6739.
[16] K. Yu et al., Dissolution of covalent adaptable network polymers in organic solvent, *Journal of the Mechanics and Physics of Solids,* 109 (2017) 78-94.
[17] F. Bedoui et al., Micromechanical modeling of isotropic elastic behavior of semicrystalline polymers, *Acata. Materialia,* 54 (2006) 1513-1523.
[18] J. A. W. V. Dommelen et al., Micromechanical modeling of the elasto-viscoplastic behavior of semi-crystalline polymers, *Journal of the Mechanics and Physics of Solids,* 51 (2003) 519-541.
[19] M. Ghasemi et al., Dissolution of semicrystalline polymer fibers: numerical modeling and parametric analysis, *AIChE Journal* (2017) 63.
[20] B. J. Lee, D. M. Parks and S. Ahzi, Micromechanical modeling of large plastic deformation and texture evolution in semicrystalline polymers, *Journal of the Mechanics and Physics of Solids*, 41 (10) (1993) 1651-1687.
[21] S. K. Mallapragada and N. A. Peppas, Crystal unfolding and chain disentanglement during semicrystalline polymer dissolution, *Aiche Journal,* 43 (4) (1997) 870-876.
[22] S. Nikolov et al., Multi-scale constitutive modeling of the small deformations of semi-crystalline polymers, *Journal of the Mechanics and Physics of Solids*, 50 (11) (2002) 2275-2302.
[23] S. Nikolov, R. A. Lebensohn and D. Raabe, Self-consistent modeling of large plastic deformation, texture and morphology evolution in semi-crystalline polymers, *Journal of the Mechanics and Physics of Solids*, 54 (7) (2006) 1350-1375.
[24] S. Felder et al., Incorparating crystallinity distributions into a thermo-mechancially coupled constitutive model for semicrystalline polymers, *International Journal of Plasticity* (2020) (In Press).
[25] J. Li, I. Romero and J. Segurado, Development of a thermo-mechanically coupled crystal plasticity modeling framework: application to polycrystalline homogenization, *International Journal of Plasticity,* 119 (2019) 313-330.
[26] A. M. Pantel et al., A thermo-mechanical large deformation constitutive model for polymers based on material network description: application to a semi-crystalline polyamide 66, *International Journal of Plasticity,* 67 (2015) 102-126.
[27] C. M. Popa et al., Formulation and implementation of a constitutive model for semicrystalline polymers, *International Journal of Plasticity,* 61 (2014) 128-156.
[28] H. Wang et al., Confined crystallinzaiton of polyethylene oxide in anolayer assemblies, *Science*, 323 (2009) 757-760.
[29] S. Cheng, D. M. Smith and C. Y. Li, How does nanoscale crystalline structure affect ion transport in solid polymer electrolyte?, *Macromolecules*, 47 (2014) 3978-3986.
[30] B. C. Hancock and G. Zografi, Characteristics and significance of the amorphous state in pharmaceutical systems, *Journal of Pharmaceutical Science,* 86 (1997) 1-12.
[31] A. Gros et al., A physically-based model for strain-induced crystallization in natural rubber, part I: life cycle of a crystallite, *Journal of the Mechanics and Physics of Solids,* 125 (2019) 164-177.
[32] J. A. W. van Dommelen et al., Micromechanical modeling of the thermo-elasto-viscoplastic behavior of semi-crystalline polymers, *Journal of the Mechanics and Physics of Solids,* 51 (3) (1999) 519-541.
[33] C. Miehe, J. Schotte and M. Lambrecht, Homogenization of inelastic solid materials at finite strains based on incremental minimization principles, Application to the texture analysis of polycrystals, *Journal of the Mechanics and Physics of Solids,* 50 (10) (2002) 2123-2167.
[34] G. Qi et al., Thermomechanical behavior of shape memory elastomeric composites, *Journal of the Mechanics and Physics of Solids,* 60 (1) (2012) 67-83.
[35] C. Yang et al., Chemo-thermomechanical behaviors of enzyme-degradable shape memory composite and its heat-enzyme triggered shape memory properties, *Computational*

Materials Science, 193 (2) (2021) 110382.
[36] Y. Mao et al., A viscoelastic model for hydrothermally activated malleable covalent network polymer and its application in shape memory analysis, *Journal of the Mechanics and Physics of Solids* (2019).
[37] S. A. Chester and L. Anand, A thermo-mechanically coupled theory for fluid permeation in elastomeric materials: Application to thermally responsive gels, *Journal of the Mechanics & Physics of Solids,* 59 (10) (2011) 1978-2006.
[38] H. Yang et al., A chemo-mechanical model of lithiation in silicon, *Journal of the Mechanics and Physics of Solids,* 70 (2014) 349-361.
[39] D. Y. Tzou, The generalized lagging response in small-scale and high-rate heating, *International Journal of Heat and Mass Transfer,* 38 (17) (1995) 3231-3240.
[40] J. K. Chen, J. E. Beraun and D. Y. Tzou, A dual-phase-lg diffusion model for interfacial layer growth in metal matrix composites, *Journal of Materials Science*, 34 (24) (1999) 6183-6187.
[41] Y. Mao et al., Thermoviscoplastic behaviors of anisotropic shape memory elastomeric composites for cold programmed non-affine shape change, *Journal of the Mechanics and Physics of Solids,* 85 (2015) 219-244.
[42] J. K. Chen, J. E. Beraun and D. Y. Tzou, A dual-phase-lag diffusion model for interfacial layer growth in metal matrix composites, *Journal of Materials Science,* 34 (24) (1999) 6183-6187.
[43] A. Sedighiamiri et al., *Micromechanical Modeling of The Deformation Kinetics of Semicrystalline Polymers*, Eindhoven: Technische Universiteit Eindhoven (2012) (Doi: 10.6100/IR735441).
[44] Q. Ge et al., Thermomechanical behavior of shape memory elastomeric composites, *Journal of the Mechanics and Physics of Solids*, 60 (1) (2012) 67-83.
[45] S. L. Buffington et al., Enzymatically triggered shape memory polymers, *Acta Biomaterialia*, 84 (2019) 88-97.
[46] V. Speranza et al., Characterization of the polycaprolactone melt crystallization: complementary optical microscopy, DSC, and AFM studies, *The Scientific World Journal* (2014).
[47] T. Patrício and P. Bártolo, Thermal stability of PCL/PLA blends produced by physical blending process, *Procedia Engineering,* 59 (2013) 292-297.
[48] J. M. Robertson, H. Birjandi Nejad and P. T. Mather, Dual-spun shape memory elastomeric composites, *ACS Macro Letters*, 4 (4) (2015) 436-440.

Appendix

A.1 1D mathematical solving of the dual-phase-lag model

The dual-lag model based diffusion model is solved by finite difference method, and described in this section. A 1D diffusion case is assumed as show in the figure and 100 difference points are applied.

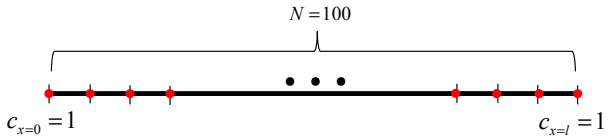

Fig. A.1. Schematic plot of 1D diffusion solving algorithm by finite difference method.

For 1D diffusion case, the diffusion equation is written as

$$\dot{c} + \tau_j \ddot{c} = \nabla \cdot \left(m \left(\nabla \otimes \mu \right) \right) + \tau_c \nabla \cdot \left(m \left(\nabla \otimes \dot{\mu} \right) \right) \tag{A.1}$$

Based on backward Euler method, the velocity and acceleration relations can be solved by

$$\begin{aligned} \ddot{c}^{(i)} &= \frac{4}{\left(\Delta t\right)^2}\left(c^{(i)} - c^{(i-1)}\right) - \frac{4}{\Delta t}\left(\dot{c}^{(i-1)}\right) - \ddot{c}^{(i-1)}, \\ \dot{c}^{(i)} &= \dot{c}^{(i-1)} + \frac{\Delta t}{2}\left(\ddot{c}^{(i-1)} + \ddot{c}^{(i)}\right) \\ \dot{c}^{(i)} &= \frac{1}{\Delta t}\left(c^{(i)} - c^{(i-1)}\right) \end{aligned} \tag{A.2}$$

Here the superscript i and $i-1$ indicates the variables of the i th iterative step and that in the last step. Using the Eq. (A.2) the Eq. (A.1) can be rewritten as

$$\begin{aligned} &\frac{1}{\Delta t}\left(c^{(i)} - c^{(i-1)}\right) + \tau_j \left(\frac{4}{\left(\Delta t\right)^2}\left(c^{(i)} - c^{(i-1)}\right) - \frac{4}{\Delta t}\left(\dot{c}^{(i-1)}\right) - \ddot{c}^{(i-1)} \right) = \\ &m \frac{\partial^2 \mu}{\partial x^2}\bigg|^{(i)} + \tau_c m \left(\frac{1}{\Delta t}\left(\frac{\partial^2 \mu}{\partial x^2}\bigg|^{(i)} - \frac{\partial^2 \mu}{\partial x^2}\bigg|^{(i-1)} \right) \right) \end{aligned} \tag{A.3}$$

The above equation can be rewritten as

$$\begin{aligned} &\left(\frac{1}{\Delta t} + \frac{4\tau_j}{\left(\Delta t\right)^2} \right) c^{(i)} - m \left(1 + \frac{\tau_c}{\Delta t} \right) \frac{\partial^2 \mu}{\partial x^2}\bigg|^{(i)} = \\ &\left(\frac{1}{\Delta t} + \frac{4\tau_j}{\left(\Delta t\right)^2} \right) c^{(i-1)} + \frac{4}{\Delta t}\tau_j \left(\dot{c}^{(i-1)}\right) + \tau_j \ddot{c}^{(i-1)} - \tau_c m \frac{1}{\Delta t} \frac{\partial^2 \mu}{\partial x^2}\bigg|^{(i-1)} \end{aligned} \tag{A.4}$$

By applying the finite difference formulations to discrete the chemical potential gradients, the above equation can be written in terms of concentrations and chemical potentials. Applying the following compatible conditions between the chemical potential and concentration,

$$\begin{aligned} &\frac{\mu^0 - \mu}{RT} + \ln\left(1 - vc\right) + vc + \chi\left(vc\right)^2 - \left(1 - f^c\right)\frac{vK}{RT}\ln\left(Jvc\right) \\ &+ \frac{\left(1 - f^c\right)}{2}\frac{vK}{RT}\ln\left(Jvc\right)^2 = 0. \end{aligned} \tag{A.5}$$

The concentration can be solved by applying above implicit

equation when given with a chemical potential. And then the concentration distribution can be solved by Eq. (A.4) finally.

A.2 Solving procedure of the uniaxial loading

Assume the applied strain loading is $\mathbf{D}=[\dot{\varepsilon},0,0;0,-\dot{\varepsilon}/2,0;0,0,-\dot{\varepsilon}/2]$ at each time interval $[t_n,t_{n+1}]$. Then the applied total macroscopic deformation is solved by

$$\mathbf{F}_{n+1}=\exp(\mathbf{D}\Delta t)\mathbf{F}_n . \tag{A.6}$$

With the deformation gradient at macroscale, the deformation gradient of each inclusion can be obtained as

$$\left(\mathbf{F}_{n+1}\right)^I=\mathbf{Q}\mathbf{F}_{n+1}\mathbf{Q}^T , \tag{A.7}$$

here $\mathbf{Q}$ is the transformation matrix between the local coordinate and the global coordinate.

At each inclusion, consider the deformation gradient is

$$\bar{\mathbf{F}}^I=\left(J^I\right)^{-1/3}\mathbf{F}^I ,\ \mathbf{L}^I=\dot{\mathbf{F}}^I\left(\mathbf{F}^I\right)^{-1} , \tag{A.8}$$

Using the relation of the $\mathbf{R}^{I_i}=\bar{\mathbf{R}}^I$, we can have $\bar{\mathbf{U}}^I=\left(J^I\right)^{-1/3}\mathbf{U}^I$. Then accordingly we can define the strain of the inclusion, the crystalline phase and the amorphous phase. Here we use the symbol $\mathbf{E}^c$, and $\mathbf{E}^a$ to denote the strain tensors. Using the relations of Eqs. (14) and (31) in the main text, we can write the constitutive relations of the crystalline phase and amorphous phase of laminated inclusion in the local coordinate by

$$\mathbf{S}^c=\mathbb{L}^c:\mathbf{E}^c ,\quad \mathbf{S}^a=\mathbb{L}^a:\mathbf{E}^a , \tag{A.9}$$

By separating the tensors in the projection subspace by $\mathbb{L}=\mathbb{L}_{\mathbf{T}}+\mathbb{L}_{\mathbf{n}}$, we can rewrite the above equations as

$$\begin{aligned}&\mathbf{S}^a_{\mathbf{n}}=\mathbb{L}^a_{\mathbf{nn}}:\mathbf{E}^a_{\mathbf{n}}+\mathbb{L}^a_{\mathbf{nT}}:\mathbf{E}^a_{\mathbf{T}} ,\ \mathbf{S}^a_{\mathbf{T}}=\mathbb{L}^a_{\mathbf{Tn}}:\mathbf{E}^a_{\mathbf{n}}+\mathbb{L}^a_{\mathbf{TT}}:\mathbf{E}^a_{\mathbf{T}} ,\\ &\mathbf{S}^c_{\mathbf{n}}=\mathbb{L}^c_{\mathbf{nn}}:\mathbf{E}^c_{\mathbf{n}}+\mathbb{L}^c_{\mathbf{nT}}:\mathbf{E}^c_{\mathbf{T}} ,\quad \mathbf{S}^c_{\mathbf{T}}=\mathbb{L}^c_{\mathbf{Tn}}:\mathbf{E}^c_{\mathbf{n}}+\mathbb{L}^c_{\mathbf{TT}}:\mathbf{E}^c_{\mathbf{T}} ,\end{aligned} \tag{A.10}$$

Using the relation of $\mathbf{E}^I_{\mathbf{T}}=\mathbf{E}^{\alpha}_{\mathbf{T}}=\mathbf{E}^c_{\mathbf{T}}$, and the constitutive relations, we can solve the $\mathbf{S}^c_{\mathbf{T}}$, $\mathbf{S}^a_{\mathbf{T}}$, $\mathbf{E}^{\alpha}_{\mathbf{T}}$ and $\mathbf{E}^c_{\mathbf{T}}$ defectively. There are still total 12 unknown variable to be solved, i.e., $\mathbf{E}^{\alpha}_{\mathbf{n}}$, $\mathbf{E}^c_{\mathbf{n}}$, $\mathbf{E}^c_{\mathbf{n}}$, $\mathbf{S}^c_{\mathbf{n}}$ and $\mathbf{S}^a_{\mathbf{n}}$. We then solve it in the following processes.

(1) Define an error function by using the stress jumping condition

$$\boldsymbol{f}^{err}=\mathbf{S}^c_{\mathbf{n}}-\mathbf{S}^a_{\mathbf{n}}\le\mathcal{E}_{\max} , \tag{A.11}$$

Using the relation of Eq. (A.10), the error function can be written as

$$\boldsymbol{f}^{err}=\left(\mathbb{L}^c_{\mathbf{nn}}:\mathbf{E}^c_{\mathbf{n}}+\mathbb{L}^c_{\mathbf{nT}}:\mathbf{E}^c_{\mathbf{T}}\right)-\left(\mathbb{L}^a_{\mathbf{nn}}:\mathbf{E}^a_{\mathbf{n}}+\mathbb{L}^a_{\mathbf{nT}}:\mathbf{E}^a_{\mathbf{T}}\right) , \tag{A.12}$$

Using the relation of $\mathbf{E}^I_{\mathbf{T}}=\mathbf{E}^{\alpha}_{\mathbf{T}}=\mathbf{E}^c_{\mathbf{T}}$, and $\mathbf{E}^a_{\mathbf{n}}=\left(\mathbf{E}^I_{\mathbf{n}}-f^c\mathbb{M}^c_{\mathbf{nn}}:\mathbf{E}^c_{\mathbf{n}}\right)/\left(1-f^c\right)$, the above error function can be rewritten as

$$\begin{aligned}\boldsymbol{f}^{err}=&\left(\mathbb{L}^c_{\mathbf{nn}}:\mathbf{E}^c_{\mathbf{n}}+\mathbb{L}^a_{\mathbf{nn}}:\frac{f^c}{(1-f^c)}\left(\mathbb{L}^c_{\mathbf{nn}}:\mathbf{E}^c_{\mathbf{n}}\right)\right)\\&+\left(\mathbb{L}^c_{\mathbf{nT}}-\mathbb{L}^a_{\mathbf{nT}}\right):\mathbf{E}^I_{\mathbf{T}}-\frac{1}{\left(1-f^c\right)}\mathbb{L}^a_{\mathbf{nn}}:\mathbf{E}^I_{\mathbf{n}}\end{aligned} . \tag{A.13}$$

(2) The above error function can be solved iteratively to obtain the $\mathbf{E}^c_{\mathbf{n}}$ and, accordingly the $\mathbf{E}^a_{\mathbf{n}}$ by

$$\mathbf{E}^a_{\mathbf{n}}=\left(\mathbf{E}^I_{\mathbf{n}}-f^c\mathbb{M}^c_{\mathbf{nn}}:\mathbf{E}^c_{\mathbf{n}}\right)/\left(1-f^c\right) . \tag{A.14}$$

Then all the strains components are solved, i.e.,

$$\mathbf{E}^a=\mathbf{E}^a_{\mathbf{n}}+\mathbf{E}^a_{\mathbf{T}},\ \mathbf{E}^c=\mathbf{E}^c_{\mathbf{n}}+\mathbf{E}^c_{\mathbf{T}} . \tag{A.15}$$

(3) The stress can be solve accordingly as

$$\mathbf{S}^a=\mathbb{L}^a:\mathbf{E}^a \text{, and } \mathbf{S}^c=\mathbb{L}^c:\mathbf{E}^c , \tag{A.16}$$

and finally,

$$\mathbf{S}^I=\left(1-f^c\right)\mathbf{S}^a+f^c\mathbf{S}^c , \tag{A.17}$$

And the stress finally in global coordinate can be solved by

$$\mathbf{S}_{PCL}=\sum_i\left[\left(\mathrm{Q}^T_{(i)}\mathbf{S}^I_{PCL(i)}\mathrm{Q}_{(i)}\right)f_i\right] , \tag{A.18}$$

where W_i is the integration weight.

A.3 Parameter identification

Four groups of model parameters are determined by calibrating the experimental results and referred to the published works: (1) 4 model parameters of temperature dependent melt-crystallization of PCL were obtain by simulation and cited from the works [44]; (2) 6 model parameters regarding chemically dependent of mass decrease fitted with degradation experimental data in a room temperature [45] and cited from the works [46, 47]; (3) 6 model parameters regarding thermomechanical properties of PCL. These parameters were determined by fitting the engineering stress-engineering strain of the PCL [48]; (4) 9 model parameters regarding thermomechanical properties of Pellethane (PE). These parameters were determined by fitting engineering stress-engineering strain of the Pellethane (PE), the storage modulus versus temperature and the tan delta versus temperature of the dry material [45, 48].

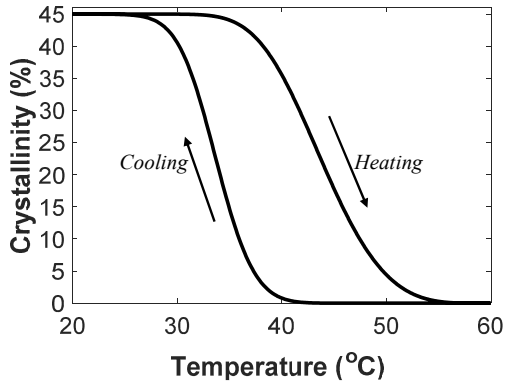

Fig. A.2. The crystallization along with the temperature variation.

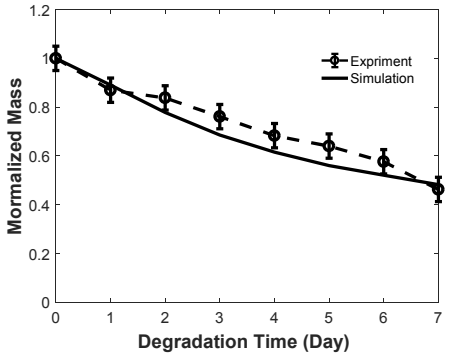

(a)

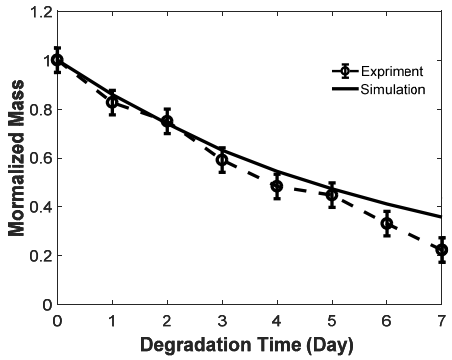

(b)

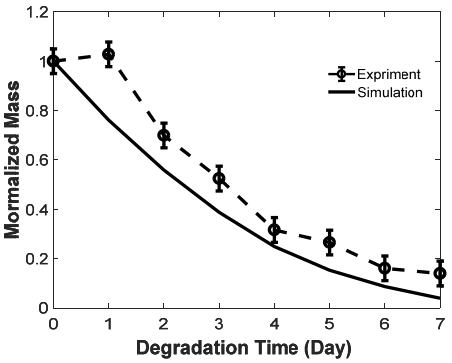

(c)

Fig. A.3. The fitted mass variation of the PCL under different enzyme concentration.

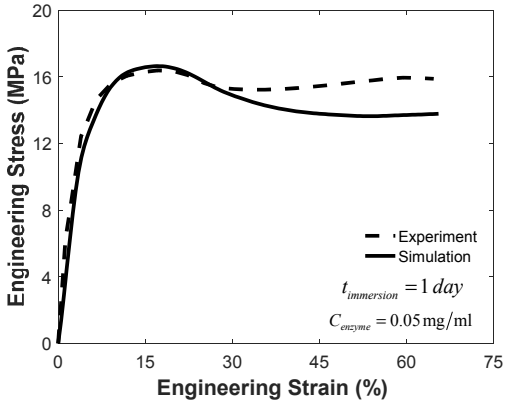

(a)

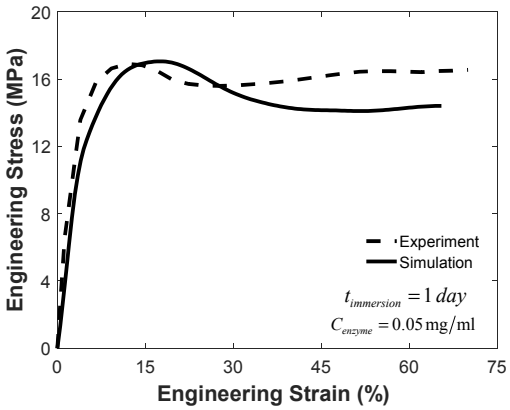

(b)

Fig. A.4. The fitted engineering stress-engineering strain of the PCL.

A.3.1 Coefficient of temperature dependent melt-crystallization of PCL $(G_0, T_\infty, k_g, E_a)$

It is necessary to capture the parameters of crystal melting kinetics because crystal melting transitions have a significant effect on the chemo-thermomechanical properties of the PCL. We use a raindrop model to simulate the crystal melting process of PCL. According to the Eq. (26) in the main text, the crystallinity of PCL can be calculated as a function of temperature. The material parameters G_0 related crystal growth rate, T_∞ is 30 K lower than T_g, k_g is nucleation constant. E_a is diffusional activation energy , these parameters are set following the work [44]. By taking these parameters, we obtained the results of the simulation are shown in Fig. A.2, it can be observed that crystallization starts at ~40 °C and finishes at ~25 °C. During the melting process, observable melting starts at ~35 °C and finishes at ~55 °C

A.3.2 Material parameters for the enzyme diffusion coefficients and enzyme-activated decrystallization of PCL, $(K_{eg}^0, K_{c0}, E_a, \Delta h_f, T_m^0, D_c)$

Parameter Δh_f is heat of fusion per unit volume of PCL, and Parameter T_m^0 is the equilibrium melting point of PCL, they are set from previous reports [46, 47], Then, by fitting the mass degradation curve of PCL at different enzyme concentra-

tions, the reference decrystallization rate K_{eg}^{0}, the reference reaction constant K_{c0}, the activation energy of the reaction constant E_a and the diffusion coefficient D_c, are fitted together, which are listed in the Table 2 in the main text. From Fig. A.3 it can be found that the simulation results using the degradation coefficients are in good agreement with the experiments.

A.3.3 Material parameters for material parameter of PCL ($N_a, N^*, \mu, K, G^c, \dot{\gamma}_0^c$)

The crosslinking density of amorphous phase N_a, number of chain segments N^*, shear modulus μ, bulk modulus K, initial yield strength G^c, reference plastic strain rate $\dot{\gamma}_0^c$, are fitted by the engineering stress-engineering strain of the PCL at room temperature. From Fig. A.4, it can be found that the simulation results using cross scale viscoplastic model are in good agreement with the experiments.

Yiqi Mao is an Associate Professor of Hunan University. He received his Ph.D. in Engineering Mechanics from Hunan University. His research interests include shape-memory polymer, self-healing materials, deformation theory and etc.